Zink, F.; Vincent, Robert Alan.
Wavelet analysis of stratosphere gravity wave packets over Macquarie Island 1. Wave parameters, Journal of Geophysical Research, 2001; 106 (D10):10275-10288.

JOURNAL OF GEOPHYSICAL RESEARCH, VOL. 106, NO. D10, PAGES 10,275–10,288, MAY 27, 2001

Wavelet analysis of stratospheric gravity wave packets over Macquarie Island
1. Wave parameters

Florian Zink and Robert A. Vincent
Department of Physics and Mathematical Physics, University of Adelaide, Adelaide, South Australia

Abstract. We describe a technique to detect gravity wave packets in high-resolution radiosonde soundings of horizontal wind and temperature. The vertical profiles of meridional and zonal wind speeds are transformed using the Morlet wavelet, and regions of high wind variance in height-wavenumber space are identified as gravity wave packets. Application of the Stokes parameter analysis to horizontal wind and temperature profiles of the reconstructed wave packets yields the wave parameters. The technique was applied to twice-daily radiosonde launches at Macquarie Island (55°S, 159°E) between 1993 and 1995. A strong seasonal cycle in the total wave variance was found, with a maximum in winter. The amount of wave energy propagating downward from the upper stratosphere also maximized in winter. Waves propagated predominately toward the southwest in winter, but in summer propagation directions were approximately isotropic. The intrinsic frequencies were close to the inertial frequency, and the waves had inferred horizontal wavelengths of several hundred kilometers.

1. Introduction

Gravity waves play an important role in driving the circulation of the atmosphere as demonstrated in numerical modeling studies [*Lindzen*, 1981; *Matsuno*, 1982; *Holton*, 1982; *Dunkerton*, 1982; *Garcia and Solomon*, 1985]. Since the resolution of general circulation models is usually too coarse to adequately resolve gravity waves, several gravity wave parameterization schemes have been developed to take these unresolved wave effects into account [*Lindzen*, 1981; *Fritts and VanZandt*, 1993; *Hines*, 1997; *Warner and McIntyre*, 1999]. These models generally require information about the gravity wave spectrum at a certain source level which is then propagated through the atmosphere. In a physically realistic model the choice of this source spectrum is influenced by experimental observations of the gravity wave field at the source height and by the agreement of the parameterized effects with measurements throughout the atmosphere.

Many experimental campaigns have been conducted to study characteristics and effects of gravity waves in the lower, middle, and upper atmosphere over the last decades. While some methods aim to directly measure the momentum fluxes associated with the gravity wave field [*Vincent and Reid*, 1983; *Fritts et al.*, 1990; *Sato*, 1994; *Alexander and Pfister*, 1995], others try to obtain information about the gravity wave activity from gravity-wave-induced perturbations of the wind and temperature fields. Radar winds have been analyzed in the lower and middle atmosphere at several locations, but the geographical coverage of these campaigns is rather sparse. The increasing use of high-resolution radiosondes for operational soundings of the lower atmosphere, on the other hand, has the potential for compiling a global climatology of gravity wave activity around the world [*Hamilton and Vincent*, 1995]. As each method can only observe a part of the gravity wave spectrum, however, different methods have to be used together to enable a better understanding of the processes involved [*Alexander*, 1998].

Methods to extract gravity wave parameters from vertical profiles of wind (and temperature) usually rely on the polarization relations for a single monochromatic gravity wave. The existence of multiple waves in the analyzed profiles might lead to erroneous results as demonstrated, for example, by *Eckermann and Hocking* [1989]. It is therefore important to ensure that only a single wave is present in the analyzed height profile. One possible step toward this goal is the decomposition of the vertical profile into different height [*Sato*, 1994] or wavelength bands [*Gonella*, 1972; *Eckermann and Vincent*, 1989; *Cho*, 1995]. The choice of a uniform width of the height or wavelength bands, however, will favor the detection of waves of a certain scale. Narrow height

Paper number 2000JD900847.
0148-0227/01/2000JD900847$09.00

bands, for example, favor the detection of waves with small vertical wavelengths, as a wave with large vertical wavelength would appear as a trend in the background wind [*Vincent et al.*, 1997]. Narrow wavelength bands, on the other hand, imply large height intervals, which opens the possibility of the coexistence of different wave packets at different heights in the vertical profile. The application of wavelet analysis can solve this dilemma to a certain extent, as it automatically adapts the window height according to the wavelength under consideration, keeping a constant ratio of wavelength to window height. The detection of wave packets by wavelet analysis is therefore a more objective means for the detection of wave packets than the decomposition of the vertical profile into uniform height or wavelength bands. Furthermore, it also yields information about the height extent of the gravity wave packets. This information will be used in a companion paper [*Zink and Vincent*] to gain some insight into source intermittency, i.e., the fraction of time the gravity wave source emits waves of a certain frequency and wavelength.

In this paper we develop a wavelet-based method to decompose vertical profiles of horizontal wind into gravity wave packets. While wavelet analysis has been applied to wind and temperature fluctuations in the atmosphere previously [*Sato and Yamada*, 1994; *Chen et al.*, 1995; *Shimomai et al.*, 1996], these studies concentrated mainly on the changes of the wavelet spectrum with time or height and less on the packet structure of the gravity wave field. section 2 gives a short definition of the wavelet transform and describes its application to the extraction of wave packets and their characteristics from radiosonde data. In section 3 we apply the algorithm to 2 years of radiosonde data from Macquarie Island and discuss the deduced gravity wave parameters. We end the paper with a short summary and conclusion in section 4. The relevant gravity wave dispersion and polarization relations are derived in Appendix A.

2. Wavelet Transform

2.1. Basic Formalism

In this section we give the definitions necessary to implement the wavelet analysis described in this paper. For a more detailed description and a review of wavelet applications in geophysics, see *Kumar and Foufoula-Georgiou* [1997, and references therein].

The term wavelets refers to a family of small waves generated from a single function $g(z)$, the so-called mother wavelet, by a series of dilations and translations. A sufficient condition for a function $g(z)$, real or complex, to qualify as a mother wavelet is admissibility,

$$c_g = \int_{-\infty}^{+\infty} \frac{|G(m)|^2}{|m|} \mathrm{d}m < \infty, \tag{1}$$

where $G(m)$ is the Fourier transform of $g(z)$. If $g(z)$ is an integrable function, it only has to be oscillatory, of finite energy, and with an average value of zero to fulfil this criterion.

The continuous wavelet transform of a real function $f(z)$ with respect to a given admissible mother wavelet $g(z)$ at scale a and dilation b is then defined as

$$W_f(a,b) = \frac{1}{a}\int_{-\infty}^{+\infty} f(z) g^*\left(\frac{z-b}{a}\right) dz, \tag{2}$$

where $a > 0$, $b \in \mathbf{R}$, and the asterisk denotes the complex conjugate. The wavelet transform gives the correlation between the original function $f(z)$ and the scaled and translated version of the mother wavelet, $g(z-b/a)$, that is, it measures how well the two signals match. The transform can also be expressed in Fourier space as

$$W_f(a,b) = \frac{1}{2\pi}\int_{-\infty}^{+\infty} G^*(am) F(m) e^{\mathrm{imb}} dm. \tag{3}$$

Admissibility is required to make sure that the original function $f(z)$ can be reconstructed from its wavelet transform without any loss of information. This reconstruction can be accomplished by summing scaled and translated versions of the mother wavelet appropriately weighted with the wavelet coefficients $W_f(a,b)$:

$$f(z) = \frac{1}{c_g}\int_0^{+\infty}\int_{-\infty}^{+\infty} W_f(a,b) g\left(\frac{z-b}{a}\right)\frac{dbda}{a^2}. \tag{4}$$

The continuous wavelet transform (2) is calculated for all points of the $a > 0, b \in \mathbf{R}$ plane and shows a high degree of redundancy. Owing to this redundancy, it is possible to reconstruct the original function using a completely different mother wavelet, e.g. the delta function, [*Farge*, 1992]:

$$f(z) = \frac{1}{c_\delta}\int_0^{+\infty} W_f(a,z)\frac{da}{a}, \tag{5}$$

where

$$c_\delta = \int_0^{+\infty} W_\delta(a,0)\frac{da}{a}. \tag{6}$$

With the normalization chosen above, the modulus square of the wavelet coefficients, $E(a,b) = |W_f(a,b)|^2$, can be interpreted as an energy density, at least for band-filter-like mother wavelets. The total energy of the signal is given by

$$E_{\mathrm{tot}} = \frac{1}{c_g}\int_0^{+\infty}\int_{-\infty}^{+\infty} E(a,b) db\frac{da}{a}. \tag{7}$$

An important point in the application of the wavelet transform to real-world data is the choice of a suitable mother wavelet. As the horizontal wind perturbations u' and v' of a gravity wave packet are essentially amplitude-modulated sine waves, the Morlet wavelet seems to be an obvious choice. It has the representations

$$g(z) = e^{i \cdot 5.4 \cdot z} e^{-\frac{z^2}{2}} \quad (8)$$

$$G(m) = \sqrt{2\pi} e^{-\frac{(m-5.4)^2}{2}} \quad (9)$$

in real and Fourier space, respectively. The factor of 5.4 ensures admissibility of the Morlet wavelet. From (1) one can see that the Fourier transform $G(m)$ has to vanish for $m = 0$ to make the integral finite. In Fourier space the Morlet wavelet is a Gaussian. Centering the Gaussian at $m = 5.4$ yields a small enough value of $G(m)$ to make the integral in (1) finite [*Kumar and Foufoula-Georgiou*, 1997].

As a progressive wavelet, the Morlet wavelet has nonzero contributions only for $m > 0$; that is. its real and imaginary parts are 90° out of phase. The relation between wavelet scale a and equivalent Fourier wavelength λ of a certain mother wavelet can be derived by wavelet transforming a sine wave of given wavelength λ [*Meyers et al.*, 1993]. In the case of the Morlet wavelet (8), it is given by $\lambda = 1.14a$.

The Morlet wavelet is not orthogonal, and the wavelet coefficients are not independent. This means that the total energy of a superposition of different wavelets is not necessarily equal to the sum of the energies of each of the wavelets. The choice of an orthogonal wavelet would resolve this problem, but one has to keep in mind that the propagation of gravity waves through the atmosphere includes nonlinear saturation effects. The proper treatment of these nonlinear effects requires knowledge about the peak amplitudes of the gravity wave packets as physical entities. While the wavelet coefficients of an orthogonal wavelet transform are independent in the mathematical sense, several of these coefficients have to be used together to represent an actual physical wave packet and to reconstruct its peak amplitude. We therefore find it more convenient to decompose the wind field using basis functions with a strong resemblance to the physical gravity wave packets. The assumed similarity of the physical wave packets with the Morlet wavelet also facilitates the extraction of wave parameters.

It is important to note that the total energy, as given by (7), is always conserved in the wavelet transform, even for nonorthogonal wavelets. As the Morlet wavelet is nonorthogonal, the sum of the square of the modulus of the wavelet coefficients does not provide the variance. Owing to the redundancy of the wavelet coefficients, the variance could be counted more than once. To get the real variance, a correction factor has to be included to take the nonorthogonality into account. This is the factor c_g in (7).

If two or more wave packets are far enough apart in wavenumber and/or height, then the wavelet coefficients occur in two clearly separated "blobs," and (7) can be used to get the variance for each packet. In the case where two packets are close in wavenumber and/or height, then some of the wavelet coefficients depend on both of the packets. The question then arises of how to distribute the variance corresponding to these coefficients. For simplicity we decided to divide the variance in equal parts between the corresponding wave packets (see end of section 2.3). This conserves total variance at the possible expense that a small fraction could be attributed to the wrong packet.

It should be pointed out that the same problem can arise with conventional Fourier analysis or with orthogonal wavelets whenever a certain wavenumber or wavelet coefficient is affected by more than one wave packet. In the case of an orthogonal wavelet, it may actually be harder to decide to which packet the variance of a certain wavelet coefficient belongs, if the mother wavelet does not show a close resemblance to the physical wave packets.

2.2. Practical Implementation

The calculation of the wavelet transform was performed in Fourier space using (3) and implemented as follows:

First, the real data series $f(z)$ is padded on both sides to avoid wraparound effects. The number of points to be added depends on the largest wavelength to be considered. Equation (2) states that the wavelet transform for a scale a at position b is given by integrating over the product of the data series $f(z)$ and the wavelet of scale a with its center at b. As the Fourier transform assumes periodicity of the transformed data series, any overhang of the wavelet at the end of the data series is wrapped around to the start of the data series, leading to undesirable contributions to the integral. If we assume the largest-scale wavelet to extend over a length of $\sim L/2$ on each side of its center, the data series has to be padded with this length to avoid any wraparound effects. This padded data series is then Fourier transformed and, for each scale a of interest, multiplied by the Fourier transform $G(am)$ of the scaled mother wavelet. Inverse Fourier transforming and unpadding then yield the complex wavelet transform $W_f(a, b)$. Its real part contains the data series $f(z)$ band-pass filtered according to scale a, and its imaginary part a 90° phase-shifted version thereof. Its modulus corresponds to the envelope of the ban-pass-filtered signal. Figure 1 gives an example of the transform of a hypothetical wind profile composed of four different wave packets using the Morlet wavelet. The result (Figure 1c) illustrates the ability of the wavelet technique to resolve wave features with very different scales.

2.3. Application to Radiosonde Data

In order to detect wave packets in the horizontal wind data, we first calculate the wavelet coefficients $W_u(a, z)$ and $W_v(a, z)$ of the vertical profiles of zonal and meridional wind components, $u(z)$ and $v(z)$, respectively. Then we scan the surface $S(a, z) = |W_u(a, z)|^2 + |W_v(a, z)|^2$ for local maxima (see Figure 1c). Only maxima exceeding a certain threshold S_{thresh} are retained in the further analysis. For each of these maxima the

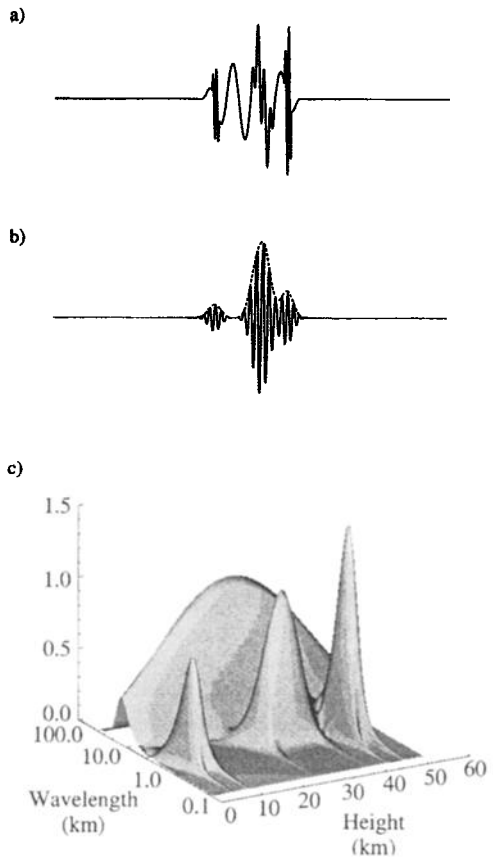

Figure 1. Example of the wavelet transform of a hypothetical wind profile using the Morlet wavelet. (a) The hypothetical wind profile, padded to avoid wraparound effects. (b) Wavelet transform of the profile in Figure 1(a) for a certain scale a. The solid line represents the real part; the dashed line represents the modulus of the transform. (c) Surface plot of the modulus of the wavelet transform as a function of wavelength and height. The four wave packets are clearly resolved.

extension of the corresponding wave packet is recorded. The boundaries (z_1, z_2 and a_1, a_2 for height and scale, respectively) are determined by scanning the surface $S(a, z)$ descending from the maximum at $(a_{\max}, z_{\max})$ until it drops to a value $1/4S(a_{\max}, z_{\max})$ or starts rising again.

The threshold value S_{thresh} was chosen as $0.01\,\text{m}^2\,\text{s}^{-2}$, which corresponds to a perturbation amplitude of 0.1 m s^{-1}. Fluctuations with amplitudes smaller than this are probably dominated by noise and are therefore neglected. While the choice of this noise threshold is somewhat arbitrary, trials have shown that the use of a smaller threshold does not change the results in any significant manner.

The wave packets can now be reconstructed using (5). Since the wavelet coefficients are only computed at discrete values for each scale a, the integral is replaced by summing the complex wavelet coefficients of all contributing scales $a_1 \ldots a_2$ at each height $z_1 \ldots z_2$ for u, v, and T. The resulting profiles now contain the isolated wave packets as their real part and their 90° phase-shifted (i.e., Hilbert transformed) version as their imaginary part. The vertical extent of each wave packet is defined as the full width at half maximum of the horizontal wind variance of the reconstructed packet.

The next step is to determine the wave parameters associated with each packet. The horizontal and vertical propagation directions are extracted by Stokes parameter analysis of the wind variations [*Vincent and Fritts*, 1987; *Eckermann and Vincent*, 1989; *Eckermann*, 1996]. The ambiguity in the horizontal propagation direction is resolved using the phase differences between temperature and horizontal perturbation velocities (see (A12)). The intrinsic frequency $\hat{\omega}$ is obtained from the ratio of the average horizontal perturbation velocities parallel and perpendicular to the wave propagation direction (A10), and the horizontal wavenumber is given by the dispersion relation (see Appendix A).

Conventional hodograph analysis uses polarization relations for a single monochromatic gravity wave to infer the intrinsic frequency and orientation of the analyzed wave packet. *Eckermann and Hocking* [1989] demonstrated that in the case of multiple wave packets the inferred intrinsic frequency can be an effect of wave superposition and might indicate azimuthal directionality in wave propagation rather than mean frequency. The wavelet-based method described here, however, isolates wave packets in wavenumber and height. Therefore the possibility of multiple wave packets in the hodograph analysis is considerably reduced compared to more traditional Fourier methods, where the whole height range is analyzed as a single wave. The analysis of a single radiosonde sounding, however, does not allow filtering of the observed oscillations in frequency. It is therefore important to keep in mind that it is not possible to distinguish different wave packets in a hodograph, if they agree in vertical wavenumber.

If two wave packets are close in height-scale space, the boundaries used to reconstruct the wave packets might overlap, i.e. certain wavelet coefficients might be used for the reconstruction of more than one wave packet. In these cases, the horizontal wind variance corresponding to these wavelet coefficients is divided between the reconstructed wave packets in equal parts in order to conserve the total wind variance.

3. Observation of Stratospheric Gravity Waves Over Macquarie Island

3.1. Radiosonde Data and Background Atmosphere

Macquarie Island (55°S, 159°E) is situated ~1500 km south of Tasmania in the subantarctic storm track. It is aligned north-south, with a length of 34 km and a maximum width of 5.5 km. Its maximum height is 433 m above sea level [*Crohn*, 1986]. The winds at Mac-

quarie Island are predominantly eastward with a high frequency of gales. A front or depression center passes the island every 5 or 6 days [*Streten*, 1988].

The Australian Bureau of Meteorology has a weather station on the north part of the island. Operational radiosonde soundings are usually performed twice daily, and the sondes reach typical heights of ~25 to 30 km. Every 2 s the radiosondes (Vaisala RS 80-15) measure the current values of pressure, temperature, and humidity. After filtering and smoothing, they are recorded at 10-s intervals at the ground station. With an average balloon ascent rate of 5 m s^{-1}, this results in a height resolution for the temperature profile of ~50 m. The finite response time of the temperature sensor attenuates high-wavenumber fluctuations, to a certain extent. Although it is possible to compensate for this effect [*Allen and Vincent*, 1995], no attempts were made in the present study. The accuracy of the temperature measurements is specified as ±0.1° C RMS. The zonal and meridional wind components, calculated from the radiosonde position over time, are reported every 10 s. After outlier removal a cubic spline is fitted over a running window of 130 s, corresponding to an actual height resolution of ~650 m. Wind fluctuations at scales smaller than this will therefore be attenuated in some way. Note that this fitting interval was changed to 250 s (1250 m) at the end of January 1994. The RMS random errors in each wind component are believed to be ~0.5 m s^{-1}. It is important to keep in mind that the different treatment of temperature and wind data can distort amplitude and phase relations between these data sets.

Owing to the finite ascent rate of the balloon, the gravity wave field undergoes changes while the profiles of wind and temperature are gathered (with an ascent rate of 5 m s^{-1} a launch to a final height of 30 km takes ~100 min), and the sonde itself experiences a horizontal drift. As we are not interested in the phase relation between packets in different height regions, we do not require different packets to be sampled simultaneously. We only require that the time taken to sample a certain coherent wave packet is small compared to its period. This seems a reasonable assumption, given that the maximum resolvable packet length is ~10 km, which is sampled in ~30 min, given an ascent rate of 5 m s^{-1}; the wave periods are of several hours duration (see below). *Gardner and Gardner* [1993] used an m^{-3} spectrum of gravity wave fluctuations in vertical wavenumber space to show that deviations from an instantaneous, vertical profile are generally small if the mean winds are less than ~50 m s^{-1}.

Figure 2 presents the monthly mean horizontal winds and temperature over the analyzed time period. The monthly mean profiles were calculated as the average over all radiosonde launches within that particular month. The zonal winds are particularly strong during winter (April to October) and reverse sign above 22 km during summer (November to March). The mean

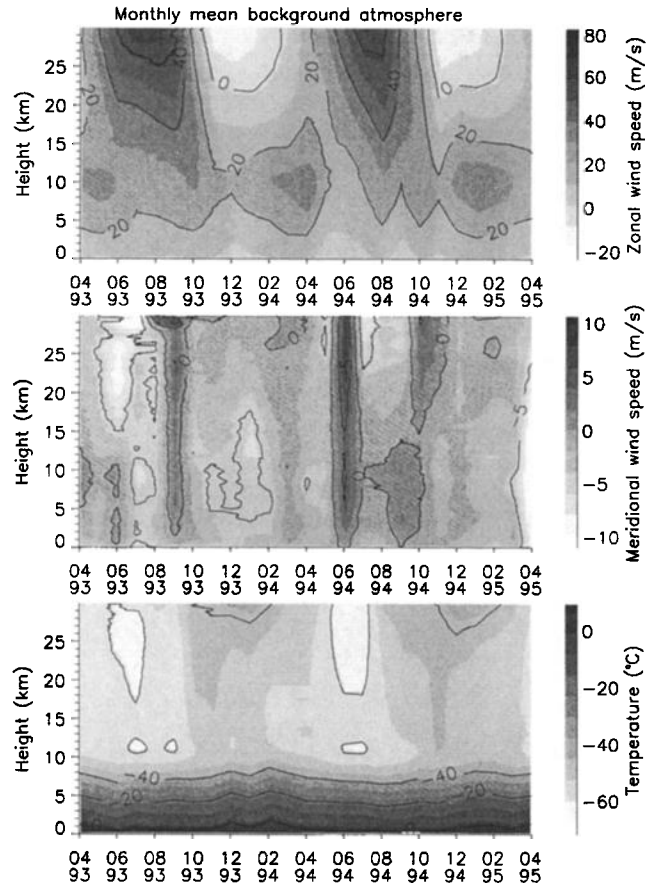

Figure 2. Monthly mean profiles of horizontal winds and temperature over Macquarie Island.

meridional winds are much weaker, with an amplitude of less than ~5 m s^{-1}. The variations in background temperature are most significant in the stratosphere, and the tropopause is at a height of ~10 km throughout the whole year.

3.2. Gravity Wave Parameters

The wavelet analysis of the gravity wave field was performed starting at a height of 12,000 m above mean sea level (MSL) using wavelengths $\lambda_i = 450. \times 2^{i/8}, i = 0 \ldots 39$. The profiles of u, v, and T were prefiltered with a fifth-order Butterworth filter with half-power points at 450 and 11,000 m or the height extent of the radiosonde data, whichever was less. The parameter S_{thresh} was selected as 0.01 m^2 s^{-2}. Results here are given as averages per radiosonde flight and function of wavelength or height. In forming these averages, the height (and therefore wavelength) coverage of the contributing radiosonde flights was taken into account.

Figure 3 shows the average monthly horizontal wind variance $\langle u'^2 + v'^2 \rangle$ as a function of height for upward and downward propagating gravity wave packets. The vertical propagation direction of the wave packets was obtained from the Stokes parameter analysis as the sense of rotation of the hodograph, with anticlockwise rotation with increasing height indicating upward en-

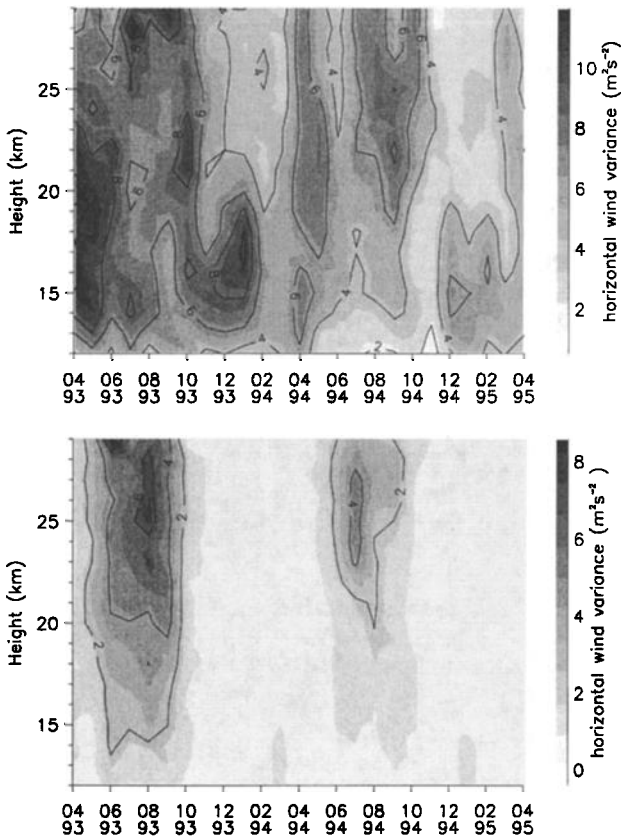

Figure 3. Monthly averaged horizontal wind variance $\langle u'^2 + v'^2 \rangle$ as a function of height and time for (top) upward and (bottom) downward propagating gravity wave packets.

ergy propagation in the Southern Hemisphere. The decrease in variance from January 1994 on is probably due to the increased phase-fitting length. Note that we here present the gravity wave activity in term s of horizontal wind variance, since this variable is directly accessible by measurement and does not depend on other inferred gravity wave parameters like, for example, wave action does.

In our analysis we will mainly concentrate on the height region from 20 to 28 km, as the waves in this region are important for the wave-mean-wind interactions in the middle and upper atmosphere. As will be seen later, waves detected below this region are filtered to a certain extent during their upward propagation. The two phases to be considered are summer (November to March) and winter (April to October). Between 40 and 60 soundings per month reached a height of above 20 km and could be used in our analysis.

Figures 4 to 6 summarize the parameters of the gravity waves detected in the height range 20 to 28 km for upward propagating gravity waves in summer and upward and downward propagating gravity waves in winter, respectively. The statistics for downward propagating gravity waves during summer are too poor to form reliable parameter estimates. Figures 4 to 6 (top) present the horizontal wind variance as a function of intrinsic horizontal propagation direction, the ground-based horizontal group velocity,

$$\mathbf{c_g} = \frac{\partial \omega}{\partial \mathbf{k}_h}, \tag{10}$$

and histograms of the ground-based zonal horizontal phase speed

$$c_{\text{phase,zonal}} = \frac{\omega}{k_h \cos(\Phi)}, \tag{11}$$

where Φ is the propagation direction in the mathematical sense, i.e., in degrees anticlockwise from east. The group velocity is important for ray-tracing studies to find the origin of the observed wave packets. For each detected wave packet, $\mathbf{c_g}$ is represented by a point in Figures 4-6 (top, middle). Figures 4 to 6 (bottom) show the horizontal wind variance of the wave field in histogram form as a function of intrinsic frequency, relative to the inertial frequency f, and vertical and horizontal wavelength, respectively. The vertical and horizontal wavelengths are binned logarithmically to take the proportionality $\Delta m \propto m$ of the wavelet analysis into account.

The observed wave field is clearly dominated by low-frequency (inertia) gravity waves, with an average horizontal wavelength of several hundred kilometers. A shift to higher intrinsic frequencies is evident in winter, when large zonal wind speeds occur. The horizontal wind variance peaks at vertical wavelengths around 4 km. Keep in mind, however, the choice of our long-wavelength cutoff of 11 km and that the filtering performed by the radiosonde equipment attenuates wavelengths less than ~1 km, so we cannot say anything about waves outside this wavelength range. The mean values of intrinsic frequency, horizontal and vertical wavelength, and ground-based zonal phase speed are given in Table 1.

3.3. Discussion

3.3.1. Seasonal variation of total gravity wave variance. A closer look at the total gravity wave horizontal wind variance and the zonal background wind speed averaged over the height range from 20 to 28 km as a function of time reveals a good correlation between these two variables (Figure 7). Both show a clear annual cycle, with maximum values of ~9 $m^2\ s^{-2}$ and 60 $m\ s^{-1}$, respectively, in July/August and minima of ~3 $m^2\ s^{-2}$ and -5 $m\ s^{-1}$, respectively, around January. A similar annual cycle of gravity wave activity has been observed at a multitude of sites in the midlatitudes and highlatitudes in both hemispheres [*Allen and Vincent*, 1995; *Eckermann et al.*, 1994]. Different mechanisms exist to explain this seasonal variability; they are described herein.

3.3.1.1. Source strength: Changes in wave generation at the source level will lead to variability in wave

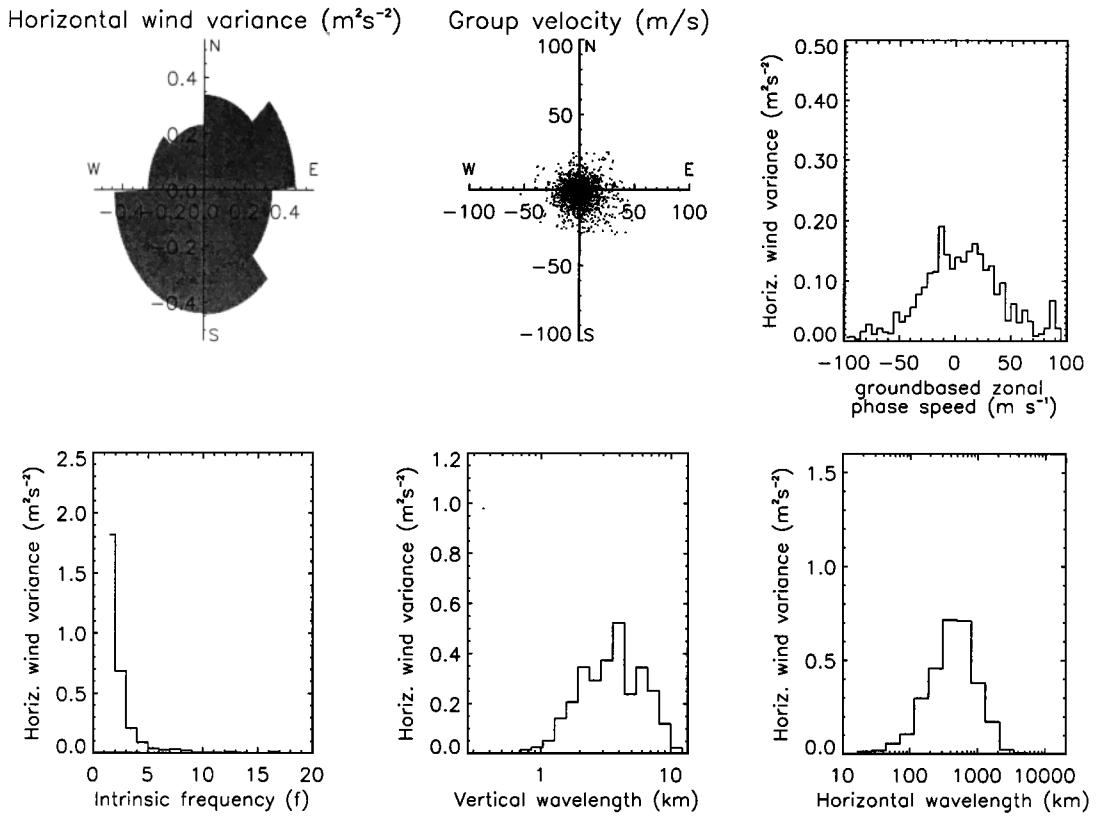

Figure 4. Parameters of upward propagating gravity waves in the height range 20 to 28 km during summer. The intrinsic frequencies are in units of the inertial frequency, f.

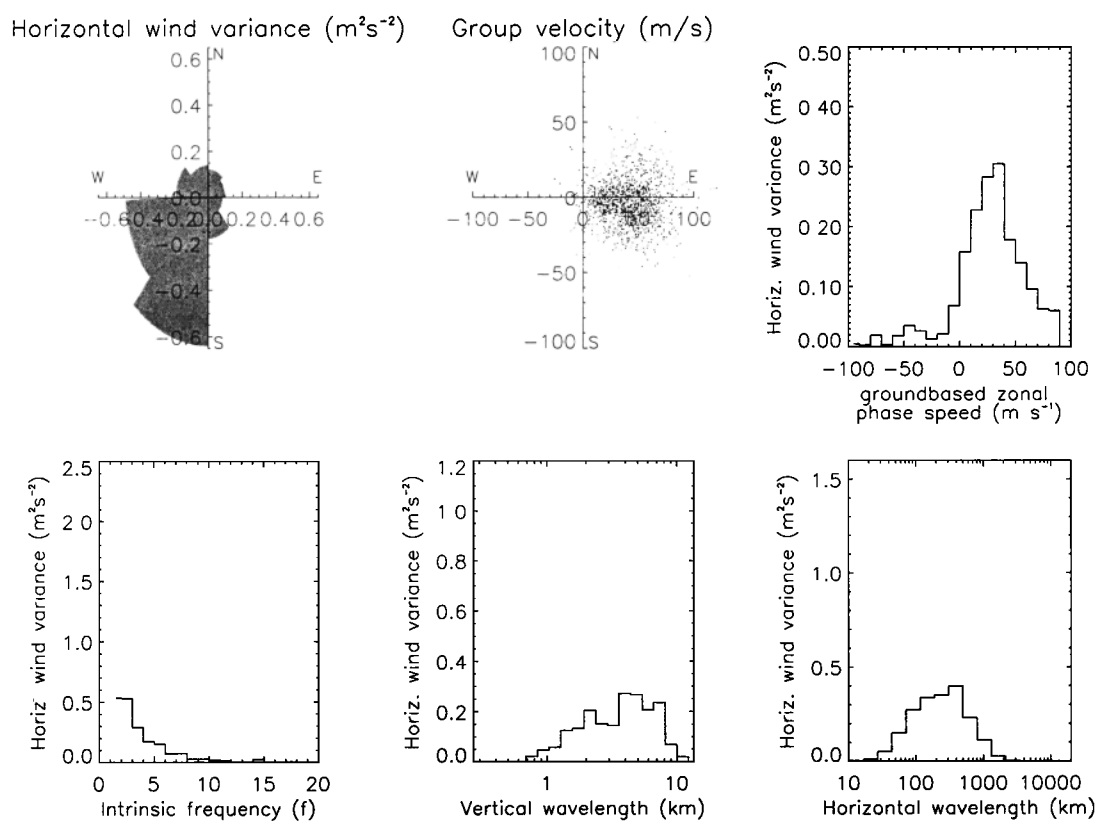

Figure 5. Same as Figure 4, but for downward propagating waves in winter.

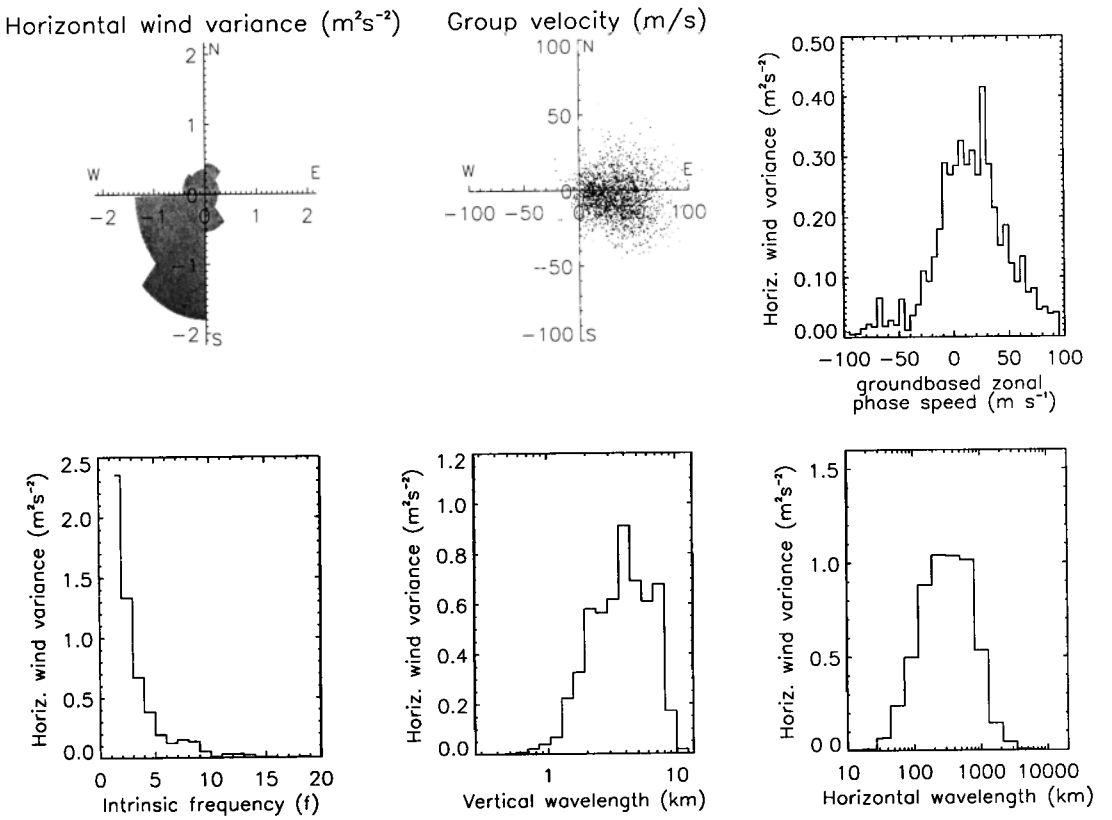

Figure 6. Same as Figure 4, but for upward propagating waves in winter.

activity at higher altitudes. Well-known sources of gravity waves in the lower atmosphere are topography [*Smith*, 1985; *McFarlane*, 1987; *Hines*, 1988; *Nastrom and Fritts*, 1992], thunderstorms [*Fovell et al.*, 1992; *Pfister et al.*, 1993; *Alexander et al.*, 1995], fronts [*Fritts and Nastrom*, 1992; *Griffiths and Reeder*, 1996; *Reeder and Griffiths*, 1996], wind shear [*Lalas and Einaudi*, 1976; *Chimonas and Grant*, 1984; *Fritts*, 1982] and geostrophic adjustment [*Schubert et al.*, 1980; *Uccellini and Koch*, 1987; *Duffy*, 1990; *Fritts and Luo*, 1992; *Luo and Fritts*, 1993; *O'Sullivan and Dunkerton*, 1995]. While topography, convection, and wind shear are believed to generate mainly high-frequency waves [*Fritts and Luo*, 1992], the most energetic gravity waves in our case study are those with frequencies close to the inertial frequency f. This is in good agreement with many other observations [*Vincent*, 1984; *Sato*, 1994; *Nastrom et al.*, 1997]. Even though the predominance of inertia-gravity waves might be an observational selection effect [*Alexander*, 1998], the observed waves could have been generated by geostrophic adjustment and frontogenesis, both of which excite waves with near-inertial frequencies [*Fritts and Luo*, 1992; *Griffiths and Reeder*, 1996; *O'Sullivan and Dunkerton*, 1995].

In the simulations of *Griffiths and Reeder* [1996] the inertia-gravity waves generated by the frontogenesis had vertical wavelengths between 2 and 10 km and horizontal wavelengths of several hundred kilometers, in good agreement with our observations. Evidence supporting geostrophic adjustment as a generation mechanism for stratospheric waves over Macquarie Island was given by *Guest et al.* [2000], who could ray trace gravity wa-

Table 1. Mean Values of Gravity Wave Parameters

	$\langle c_{\text{phase,zonal}} \rangle$ (m s^{-1})	$\langle \hat{\omega} \rangle$	$2\pi/\langle m \rangle$ (km)	$2\pi/\langle k_h \rangle$ (km)
Winter, upward	15.3	3.1	4.2	431
Winter, downward	27.1	3.7	4.1	319
Summer, upward	6.4	2.3	3.9	547

Variables are defined as follows: $\langle c_{\text{phase,zonal}} \rangle$, ground-based phase speed; $\langle \hat{\omega} \rangle$, intrinsic frequency in units of f; $2\pi/\langle m \rangle$, vertical wavelength; $2\pi/\langle k_h \rangle$, horizontal wavelength.

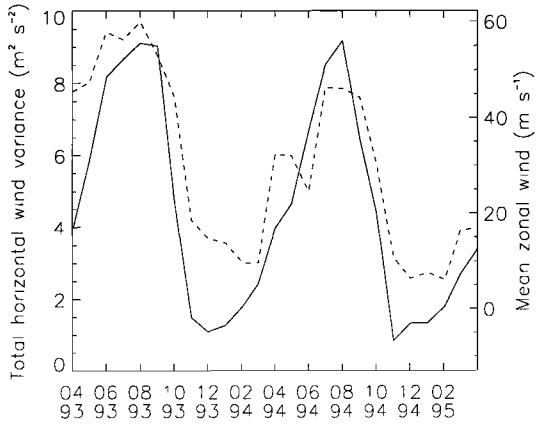

Figure 7. Total horizontal gravity wave wind variance (dashed curve) and zonal background wind speed (solid curve) averaged over the height range from 20 to 28 km as a function of time.

ves observed during a campaign in October 1994 backward in time to their origins near the polar jet at the tropopause.

3.3.1.2. Background atmosphere: If we assume no explicit dependence of the background atmosphere on horizontal position x and y and time t, then the horizontal wavenumbers k and l and the ground-based frequency ω are constant along the ray of each wave packet. The intrinsic frequency $\hat{\omega}$ as a function of height is then

$$\hat{\omega}(z) = \omega - u(z)k - v(z)l, \tag{12}$$

and the vertical wavenumber $m(z)$ is given via the dispersion relation. In summer $du/dz < 0$ and waves propagating westward ($k < 0$) are Doppler shifted to lower intrinsic frequencies as they reach higher levels. Their vertical wavelength therefore decreases with height. If their intrinsic frequencies drops below the inertial frequency f, these waves will be critically filtered. In winter, on the other hand, $du/dz > 0$ and westward propagating waves are Doppler shifted to higher intrinsic frequencies and longer vertical wavelengths. If their intrinsic frequency reaches the turning frequency, at which m becomes zero, these waves will be reflected. Owing to the limited bandwidth of our analysis methods, however, waves will be shifted out of the observable vertical wavelength range before they encounter critical or turning levels. Nevertheless, the effect of critical level filtering can be observed in the horizontal wind variance for upward propagating waves during summer at a height of ~20 km, where the zonal wind reverses sign (Figure 3, top). Observations of similar modulation of gravity wave variance by the background wind were made by *Whiteway and Duck* [1996, 1999].

The wind variance of a wave packet will change, even if it is shifted within the observable vertical wavelength range. In the absence of dissipation, the amplitude of a wave packet along its ray is determined by the conservation of wave action flux [*Lighthill*, 1978]

$$A_f = c_{g,z}\frac{E}{\hat{\omega}} = \text{const}, \tag{13}$$

where $c_{g,z}$ is the vertical group velocity and E is the total energy density,

$$E = \frac{1}{2}\rho(\overline{u'^2} + \overline{v'^2} + \overline{w'^2} + N^2\overline{\zeta'^2}). \tag{14}$$

Here ζ' is the wave-induced vertical displacement of the air parcel from its equilibrium. Owing to the density decreasing exponentially with height, the horizontal perturbation velocity of a wave with constant intrinsic frequency grows exponentially in amplitude. If the intrinsic frequency is increasing with height, however, the (horizontal) wave amplitude will grow less than exponentially; if it is decreasing with height, it will grow more than exponentially. *Eckermann* [1995a] used this effect of background winds on vertical wavenumber spectra to explain the occurrence of attenuated spectra in several experimental observations. He was also able to model seasonal changes in wave activity due to variability in background temperature and hence density [*Eckermann*, 1995b]. Similarly, *Alexander* [1998] could explain the variations in gravity wave activity at midlatitudes with effects of the background atmosphere on a constant source spectrum.

The observed seasonal dependence of gravity wave activity is, therefore, not necessarily indicative of source variability and might be largely explained by the propagation of a constant source spectrum through a variable background atmosphere.

3.3.2. Seasonal variation of downward propagating gravity wave variance. As mentioned above, increased wind speed will shift the intrinsic frequency of gravity waves propagating against the wind to larger values. Such a shift of the intrinsic frequency distribution to higher values is evident in winter from Figures 4 to 6. If the wind speed and hence the frequency shift is large enough some waves will reach their turning fre-

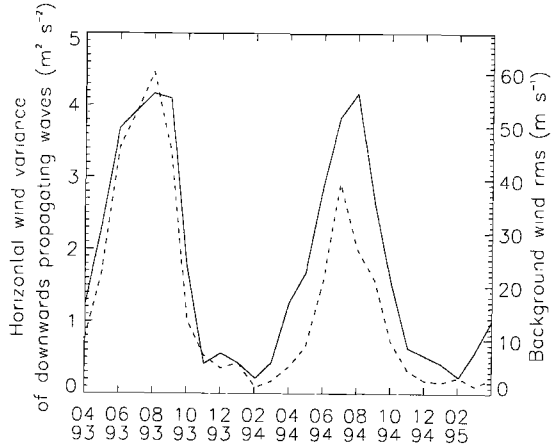

Figure 8. Horizontal wind variance of downward propagating gravity waves (dashed curve) and absolute background wind speed (solid curve) as functions of time.

quencies and be reflected. Figure 8 reveals a good correlation between the absolute background wind speed and the horizontal wind variance of the downward propagating waves as a function of time. For background wind speeds of ~50 m s^{-1} during the stratospheric winter jet, the horizontal wind variance reaches values of up to 4 m^2 s^{-2}, while the wave activity almost ceases during summer, when the atmosphere in the analyzed height range is basically at rest.

Using the rotary spectral method, *Allen* [1996] found a similar increase in the fraction of clockwise rotating wind component during winter, when strong mean winds prevail in the stratosphere over Macquarie Island. Following *Eckermann et al.* [1994], Allen, however, attributed this increase to a change in frequency distribution rather than to ratio of downward to upward propagating gravity wave energy. He argued that the intrinsic frequency of an upward propagating, zonally aligned gravity wave is Doppler shifted by the zonal mean winds. This Doppler shifting to higher frequencies reduces the axial ratio of the hodograph ellipse and results in an increased fraction of clockwise rotation. Even though the wave packet is upward propagating, rotary spectral analysis would regard that fraction of its horizontal wind variance as downward propagating [*Vincent*, 1984]. In our analysis, however, the total horizontal wind variance is counted as either upward or downward propagating, depending on the anticlockwise or clockwise sense of rotation of the hodograph, i.e., the sign of the Stokes parameter Q. Therefore the argument of *Eckermann et al.* [1994] can no longer be applied; we believe that in our case we really deal with downward propagating gravity waves.

It is important to note that wave reflection can occur at frequencies much lower than the buoyancy frequency N, if the density height terms are retained in the dispersion relation (A7), i.e., if the Boussinesq approximation is not applied. Figure 9 shows the turning frequency as a function of horizontal wavelength for a density scale height of 6500 m and a buoyancy frequency of 0.02rad s at Macquarie Island for a compressible (dashed curve, c_s = 300 m s^{-1}) and incompressible (solid curve) atmosphere.

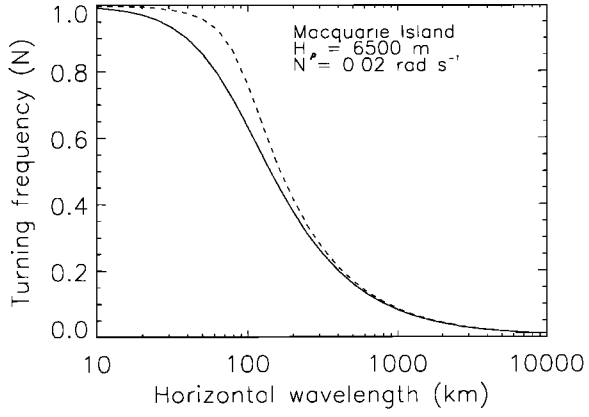

Figure 9. Turning frequency as a function of horizontal wavelength for a density scale height of 6500 m and a buoyancy frequency of 0.02rad s at Macquarie Island for a compressible (dashed curve, c_s = 300 m s^{-1}) and incompressible (solid curve) atmosphere.

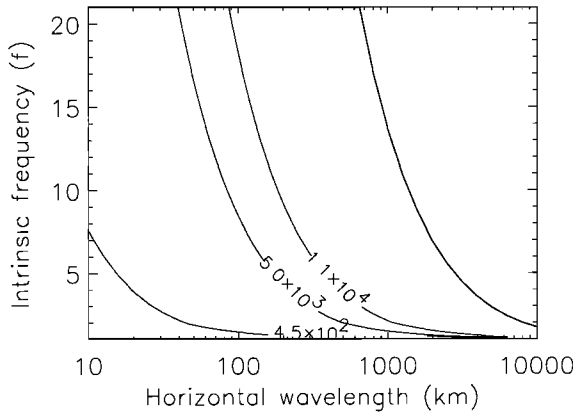

Figure 10. Contour plot of vertical wavelength as a function of horizontal wavelength and intrinsic frequency. The numbers on the contour lines are the vertical wavelength in meters. The rightmost curve corresponds to the turning frequency.

ing frequency as a function of horizontal wavelength for a density scale height of 6500 m and a buoyancy frequency of 0.02 rad s^{-1} at Macquarie Island for a compressible (dashed curve) and incompressible (solid curve) atmosphere. The turning frequency at horizontal wavelengths of several hundred kilometers, as observed in this study, is reduced to as little as one tenth of the buoyancy frequency N. The local buoyancy frequency encountered by a wave propagating through the atmosphere can be substantially reduced compared to the mean background value by waves of large vertical wavelength. These large vertical wavelength waves can act as a background atmosphere for waves of smaller vertical wavelength, in a manner similar to that described by *Hines* [1991]. The observed variation in wind variance of downward propagating waves might thus be explained by reflection of waves from levels of high background wind speed and low local buoyancy frequency.

The percentage of downward propagating gravity waves with approximately zero phase speed is significantly smaller than that for upward propagating waves in winter (Figure 5). This could indicate generation of downward propagating waves by geostrophic adjustment of the stratospheric jet. In such a case one expects ground-based zonal phase velocities of the generated waves to be close to the zonal background velocity, as the waves have to be generated close to a critical level. It is noteworthy that gravity waves appearing in high-resolution general circulation model (GCM) simulations [*Sato et al.*, 1999] and in radiosonde observations at polar latitudes in the Southern Hemisphere [*Yoshiki and Sato*, 2000] appear to be generated by the polar night jet in the stratosphere.

3.3.3. Preponderance of low-frequency gravity waves. As seen above, inclusion of the density height terms in the dispersion relation can significantly reduce the range of intrinsic frequencies over which wave propagation is possible. If we furthermore con-

sider the imposed wavelength cutoff at a vertical wavelength of 11,000 m, the maximum observable intrinsic frequency as a function of horizontal wavelength is again drastically reduced (Figure 10). The preponderance of inertia-gravity waves in our data could therefore be an observational selection effect. On the other hand, it could be understood if the main generation mechanisms are frontogenesis and geostrophic adjustment, as indicated above.

Topography, however, is another possible generation mechanism at Macquarie Island, which may generate high intrinsic frequency waves. We do not believe that topography is a significant source for the waves we see for the following reasons. *Schoeberl* [1985] calculated the dominant horizontal wavelength of the gravity wave spectrum forced by a bell-shaped mountain ridge of equivalent mountain half-width a as $2\pi a$. Considering the prevailing eastward winds at ground level at Macquarie Island and a half width of the island between 1 and 2 km, the dominant horizontal wavelength lies between ~6 and 13 km. The minimum horizontal wavelength of zonally aligned, stationary (that is, $\omega = 0$) gravity waves that can propagate through a gradually changing background atmosphere is obtained from (12) and (A7) with $\omega = l = 0$, that is,

$$\lambda_{h,\min} = 2\pi u/N, \tag{15}$$

resulting in a minimum horizontal wavelength of mountain waves in the lower stratosphere over Macquarie Island of around 15 km. A significant portion of the generated mountain waves is therefore likely to be trapped in the troposphere and unlikely to contribute to our studies.

3.3.4. Propagation directions. The variance-weighted intrinsic propagation direction of the observed gravity wave packets is predominantly south-southwestward during winter and nearly isotropic during summer, as illustrated in Figures 4 to 6. In interpreting these observations, one has to take the effects of the background atmosphere into account. For the strong zonal winds in winter, zonally propagating gravity waves experience large shifts in intrinsic frequency and vertical wavenumber and can be shifted into and out of the observable vertical wavenumber range. Thus we anticipate some anisotropy in the zonal direction even for an isotropic source spectrum. Owing to the low prevailing meridional winds it is hard to explain the meridional anisotropy by conditions of the background atmosphere or as an observational selection effect. The observed anisotropy, however, does not imply anisotropic gravity wave generation, but it could also be due to a latitudinally confined source located north of Macquarie Island.

3.3.5. Wave amplitudes and saturation. Gravity waves will only affect the background flow or lead to mixing of constituents in the atmosphere if wave dissipation occurs. Dynamical and convective instability are thought to be the main dissipation processes [*Fritts and Rastogi*, 1985], although other mechanisms do exist (molecular diffusion, radiative damping, nonlinear interactions). Convective and dynamic instability lead to breaking of a wave, if its amplitude exceeds a certain threshold. Owing to the transverse shear in the velocity field of low-frequency gravity waves the wave amplitude required for dynamic instability falls well below that necessary for convective instability as $f/\hat{\omega} \to 1$ [*Fritts and Rastogi*, 1985]. The threshold amplitude for dynamical instability is [*Fritts*, 1989]

$$u'_{||,\mathrm{sat}} = \frac{2\sqrt{1-\frac{f^2}{\hat{\omega}^2}}}{1+\sqrt{1-\frac{f^2}{\hat{\omega}^2}}} c_{\mathrm{phase,intrinsic}}. \tag{16}$$

Owing to the existence of threshold amplitudes, these saturation mechanisms are nonlinear, and the knowledge of actual wave amplitudes is important when the effect of gravity waves on the background atmosphere is to be assessed. Figure 11 shows a contour plot of normalized horizontal wind variance as a function of perturbation amplitude $u'_{||}$ and saturation amplitude $u'_{||,\mathrm{sat}}$ for gravity waves observed at Macquarie Island during summer and winter between heights of 20 and 28 km. Only soundings after February 1994 were considered to ensure identical filtering of the radiosonde data. In both summer and winter the vast majority of the observed

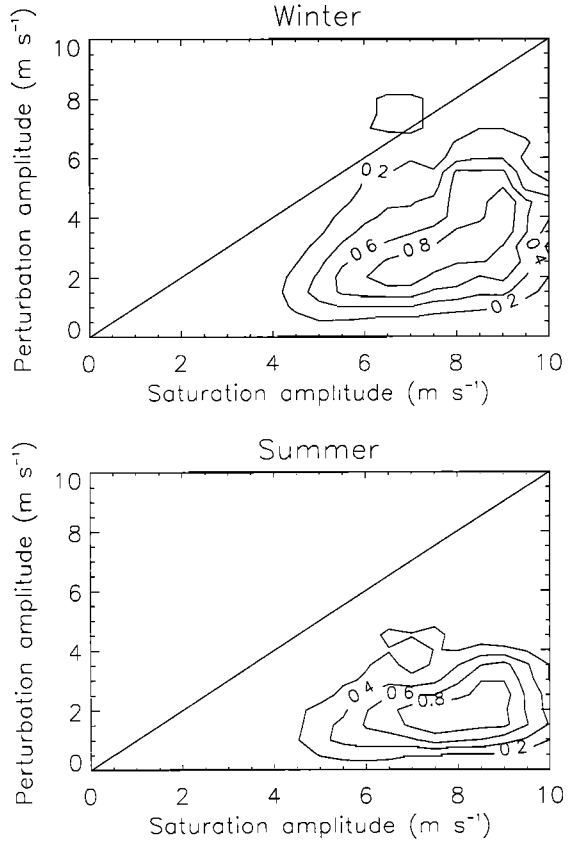

Figure 11. Normalized horizontal wind variance as function of perturbation amplitude $u'_{||}$ and saturation amplitude $u'_{||,\mathrm{sat}}$ for summer and winter between heights of 20 and 28 km.

waves have perturbation amplitudes less than the saturation amplitude computed according to (16). The amplitudes of these waves are therefore either too small to reach the threshold for dynamic instability within the analyzed height range or have already been dissipated.

4. Summary and Conclusion

A method to extract gravity wave packets from vertical profiles of horizontal wind and temperature is presented. Using wavelet analysis, we are able to separate the wave field in height and wavelength and, therefore, to reduce the presence of multiple waves in the hodograph analysis. Furthermore, we get information about the height extent of the wave packets. The Morlet wavelet was chosen to decompose the wave field into basis functions that are similar to the assumed physical gravity wave packets. This allows a simple reconstruction of the actual wave packet amplitude, an important issue when nonlinear saturation effects are considered.

Application of the method to twice-daily radiosonde soundings of the lower stratosphere over Macquarie Island revealed a strong seasonal cycle in the total and downward propagating gravity wave variance with a maximum in winter. This maximum in gravity wave variance coincides with a shift of the wave amplitude distribution to larger values. The variance-weighted intrinsic propagation direction during winter is predominantly southsouthwestward, while it is nearly isotropic during summer. The observed wave field was found to be dominated by low-frequency inertia-gravity waves.

In the interpretation of these findings, attention was paid to the limited vertical wavelength range observable with the radiosonde technique [*Alexander*, 1998]. Doppler shifting of waves into and out of this wavelength band can lead to significant changes in the observed wave field and complicates the analysis. The usefulness of the presented observations is therefore mainly in conjunction with modeling studies. In the present paper, the wave characteristics were presented in terms of variables that are directly accessible by measurements, i.e., vertical wavelength and wind variance. A disadvantage of this approach is that these variables undergo changes as the wave packet is Doppler shifted by changes in the background wind with height and therefore they depend on the detection level of the wave packet.

In a companion paper [*Zink and Vincent*, this issue] we express the wave characteristics by invariants under the propagation of the wave packet through a steady state atmosphere and use these parameters to assess the effect of the observed wave field on the lower and middle atmosphere by ray-tracing studies.

Appendix A: Dispersion and Polarization Relations

Ignoring gradients in the background flow $\mathbf{u}$ by setting $\mathbf{u}(z) = (u_0, v_0, 0)$, the linearized momentum, continuity, and ideal gas equations for a compressible, inviscid atmosphere become

$$\frac{Du'}{Dt} - fv' = -\frac{1}{\rho_o}\frac{\partial p'}{\partial x}, \quad \text{(A1a)}$$

$$\frac{Dv'}{Dt} + fu' = -\frac{1}{\rho_o}\frac{\partial p'}{\partial y}, \quad \text{(A1b)}$$

$$\frac{Dw'}{Dt} = -\frac{1}{\rho_o}\frac{\partial p'}{\partial z} - \frac{\rho'}{\rho_o}g. \quad \text{(A1c)}$$

$$\frac{D\rho'}{Dt} + w'\frac{\partial \rho_o}{\partial z} + \rho_o \mathrm{div}\mathbf{u}' = 0, \quad \text{(A2)}$$

$$\frac{Dp'}{Dt} + w'\frac{\partial p_o}{\partial z} - c_s^2\left(\frac{d\rho'}{dt} + w'\frac{\partial \rho_o}{\partial z}\right) = 0. \quad \text{(A3)}$$

Here $D/Dt = \partial/\partial t + \mathbf{u}\nabla$ is the total (Lagrangian) derivative and $\mathbf{u}' = (u', v', w')$, p', and ρ' are the perturbation velocities, pressure, and density, respectively. p_o and ρ_o designate background pressure and density, respectively; which are assumed to only vary with height; f is the Coriolis parameter; g is the gravitational acceleration; and c_s is the speed of sound.

Substituting solutions of the form

$$\begin{pmatrix} u' \\ v' \\ w' \end{pmatrix} = \rho_o^{-1/2}\begin{pmatrix} \hat{u} \\ \hat{v} \\ \hat{w} \end{pmatrix}\exp i(\mathbf{kx} - \omega t), \quad \text{(A4)}$$

$$\begin{pmatrix} p' \\ \rho' \end{pmatrix} = \rho_o^{+1/2}\begin{pmatrix} \hat{p} \\ \hat{\rho} \end{pmatrix}\exp i(\mathbf{kx} - \omega t), \quad \text{(A5)}$$

where $\mathbf{k} = (k, l, m)$ and $\mathbf{x} = (x, y, z)$, and expressing the intrinsic frequency in a reference frame following the background flow as

$$\hat{\omega} = \omega - \mathbf{ku} \quad \text{(A6)}$$

yields the nonhydrostatic dispersion relation

$$m^2 = \frac{N^2 - \hat{\omega}^2}{\hat{\omega}^2 - f^2}(k^2 + l^2) - \frac{1}{4H_\rho^2} + \frac{\hat{\omega}^2}{c_s^2}. \quad \text{(A7)}$$

Here

$$N^2 = -\frac{g}{\rho_o}\frac{\partial \rho_o}{\partial z} - \frac{g^2}{c_s^2} \quad \text{(A8)}$$

is the buoyancy or Brunt-Väisäla frequency and

$$H_\rho = \frac{1}{\rho_o}\frac{\partial \rho_o}{\partial z} \quad \text{(A9)}$$

the density scale height. The dispersion relation (A7) also includes an acoustic branch. For an incompressible atmosphere, acoustic waves can be excluded by letting $c_s \to \infty$. Further omission of the second term in (A7) results in the Boussinesq approximation, a short-wavelength approximation valid for $m \gg 1/2H_\rho$. This is the approximation used throughout this paper, unless noted otherwise.

The polarization relations are simplified in a coordinate system aligned with the propagation direction of the wave. Let $u'_{||}$ and $v'_{\perp}$ designate the horizontal perturbation velocities parallel and perpendicular, respectively, to the wave vector. The relevant polarization equations in the Boussinesq approximation then become

$$v'_{\perp} = -i\frac{f}{\hat{\omega}}u'_{||}, \quad \text{(A10)}$$

$$w' = -\frac{k_h}{m}u'_{||}, \quad \text{(A11)}$$

$$\hat{T}' = \frac{T'}{T_o} = i\frac{N^2}{g\hat{\omega}}\frac{k_h}{m}u'_{||}, \quad \text{(A12)}$$

where T' and T_o are the perturbation and background temperature, respectively, and k_h is the horizontal wavenumber.

Acknowledgments. The authors would like to thank Joan Alexander for corrections and comments to an earlier version of this manuscript. We acknowledge the provision of the radiosonde data by the Australian Bureau of Meteorology.

References

Alexander, M. J., Interpretations of observed climatological patterns in stratospheric gravity wave variance, *J. Geophys. Res.*, *103*, 8627–8640, 1998.

Alexander, M. J., and L. Pfister, Gravity wave momentum flux in the lower stratosphere over convection, *Geophys. Res. Lett.*, *22*, 2029–2032, 1995.

Alexander, M. J., J. R. Holton, and D. R. Durran, The gravity wave response above deep convection in a squall line simulation, *J. Atmos. Sci.*, *52*, 2212–2226, 1995.

Allen, S. J., Gravity wave motions in the troposphere and lower stratosphere, Ph.D. thesis, Univ. of Adelaide, Adelaide, South Aust., 1996.

Allen, S. J., and R. A. Vincent, Gravity wave activity in the lower atmosphere: Seasonal and latitudinal variations, *J. Geophys. Res.*, *100*, 1327–1350, 1995.

Chen, K. Y., I. J. Fu, S. Y. Su, and C. H. Liu, Wavelet analysis on transient behavior of wind fluctuations observed by MST radar, *Radio Sci.*, *30*, 1111–1123, 1995.

Chimonas, G., and J. R. Grant, Shear excitation of gravity waves, II, upscale scattering from Kelvin-Helmholtz waves, *J. Atmos. Sci.*, *41*, 2278–2288, 1984.

Cho, J. Y. N., Inertio-gravity wave parameter estimation from cross-spectral analysis, *J. Geophys. Res.*, *100*, 18,727–18,737, 1995.

Crohn, P. W., The geology and geomorphology of Macquarie Island with special emphasis on heavy metal trace element distribution, *ANARE Research Notes*, *39*, 1986.

Duffy, D. G., Geostrophic adjustment in a baroclinic atmosphere, *J. Atmos. Sci.*, *47*, 457–473, 1990.

Dunkerton, T. J., Theory of the mesopause semiannual oscillation, *J. Atmos. Sci.*, *39*, 2681–2690, 1982.

Eckermann, S. D., Effect of background winds on vertical wavenumber spectra of atmospheric gravity waves, *J. Geophys. Res.*, *100*, 14,097–14,112, 1995a.

Eckermann, S. D., On the observed morphology of gravity-wave and equatorial-wave variance in the stratosphere, *J. Atmos. Sol. Terr. Phys.*, *57*, 105–134, 1995b.

Eckermann, S. D., Hodographic analysis of gravity waves: Relationships among Stokes parameters, rotary spectra and cross-spectral methods, *J. Geophys. Res.*, *101*, 19,169–19,174, 1996.

Eckermann, S. D., and W. K. Hocking, Effect of superposition on measurements of atmospheric gravity waves: A cautionary note and some reinterpretations, *J. Geophys. Res.*, *94*, 6333–6339, 1989.

Eckermann, S. D., and R. A. Vincent, Falling sphere observations of anisotropic gravity wave motions in the upper stratosphere over Australia, *Pure Appl. Geophys.*, *130*, 509–532, 1989.

Eckermann, S. D., I. Hirota, and W. K. Hocking, Gravity wave and equatorial wave morphology of the stratosphere derived from long-term rocket soundings, *Q. J. R. Meteorol. Soc.*, *121*, 149–186, 1994.

Farge, M., Wavelet transforms and their applications to turbulence, *Annu. Rev. Fluid Mech.*, *24*, 395–457, 1992.

Fovell, R., D. Durran, and J. R. Holton, Numerical simulations of convectively generated stratospheric gravity waves, *J. Atmos. Sci.*, *49*, 1427–1442, 1992.

Fritts, D. C., Shear excitation of atmospheric gravity waves, *J. Atmos. Sci.*, *39*, 1936–1952, 1982.

Fritts, D. C., A review of gravity wave saturation processes, effects, and variability in the middle atmosphere, *Pure Appl. Geophys.*, *130*, 343–371, 1989.

Fritts, D. C., and Z. Luo, Gravity wave excitation by geostrophic adjustment of the jet stream, I, two-dimensional forcing, *J. Atmos. Sci.*, *49*, 681–697, 1992.

Fritts, D. C., and G. D. Nastrom, Sources of mesoscale variability of gravity waves, II, frontal, convective, and jet stream excitation, *J. Atmos. Sci.*, *49*, 681–697, 1992.

Fritts, D. C., and P. K. Rastogi, Convective and dynamical instabilities due to gravity wave motions in the lower and middle atmosphere: Theory and observations, *Radio Sci.*, *20*, 1247–1277, 1985.

Fritts, D. C., and T. E. VanZandt, Spectral estimates of gravity wave energy and momentum fluxes, i, Energy dissipation, acceleration and constraints, *J. Atmos. Sci.*, *50*, 3685–3694, 1993.

Fritts, D. C., T. Tsuda, T. E. VanZandt, S. A. Smith, T. Sato, S. Fukao, and S. Kato, Studies of velocity fluctuations in the lower atmosphere using the MU radar, II, Momentum fluxes and energy densities, *J. Atmos. Sci.*, *47*, 51–66, 1990.

Garcia, R. R., and S. Solomon, The effect of breaking gravity waves on the dynamics and chemical composition of the mesosphere and lower thermosphere, *J. Geophys. Res.*, *90*, 3850–3860, 1985.

Gardner, C. S., and N. F. Gardner, Measurement distortion in aircraft, space shuttle, and balloon observations of atmospheric density and temperature perturbation spectra, *J. Geophys. Res.*, *98*, 1023–1033, 1993.

Gonella, J., A rotary-component method for analysing meteorological and oceanographic vector time series, *Deep Sea Res.*, *19*, 833–846, 1972.

Griffiths, M., and M. J. Reeder, Stratospheric inertia-gravity waves generated in a numerical model of frontogenesis I, Model solutions, *Q. J. R. Meteorol. Soc.*, *122*, 1153–1174, 1996.

Guest, F. M., M. J. Reeder, C. J. Marks, and D. J. Karoly, Inertia-gravity waves observed in the lower stratosphere over Macquarie Island, *J. Atmos. Sci.*, *57*, 737–752, 2000.

Hamilton, K., and R. A. Vincent, High-resolution radiosonde data offer new prospects for research, *EoS Trans. AGU*, *76*, 497, 1995.

Hines, C. O., A modeling of atmospheric gravity waves and wave drag generated by isotropic and anisotropic terrain, *J. Atmos. Sci.*, *45*, 309–322, 1988.

Hines, C. O., The saturation of gravity waves in the middle atmosphere, II, Development of Doppler-spread theory, *J. Atmos. Sci.*, *48*, 1360–1379, 1991.

Hines, C. O., Doppler-spread parametrization of gravity-wave momentum deposition in the middle atmosphere, 1,

Basic formulation, *J. Atmos. Sol. Terr. Phys.*, *59*, 371–386, 1997.

Holton, J. R., The role of gravity wave induced drag and diffusion in the momentum budget of the mesosphere, *J. Atmos. Sci.*, *39*, 791–799, 1982.

Kumar, P., and E. Foufoula-Georgiou, Wavelet analysis for geophysical applications, *Rev. Geophys.*, *35*, 385–412, 1997.

Lalas, D. P., and F. Einaudi, On characteristics of gravity waves generated by atmospheric shear layers, *J. Atmos. Sci.*, *33*, 1248–1259, 1976.

Lighthill, J., *Waves in Fluids*, Cambridge Univ. Press, New York, 1978.

Lindzen, R. S., Turbulence and stress owing to gravity wave and tidal breakdown, *J. Geophys. Res.*, *86*, 9707–9714, 1981.

Luo, Z., and D. C. Fritts, Gravity-wave excitation by geostrophic adjustment of the jet stream, II, Three-dimensional forcing, *J. Atmos. Sci.*, *50*, 104–115, 1993.

Matsuno, T., A quasi one-dimensional model of the middle atmosphere circulation interacting with internal gravity waves, *J. Meteorol. Soc. Jpn.*, *60*, 215–226, 1982.

McFarlane, N. A., The effect of orographically excited gravity wave drag on the general circulation of the lower stratosphere and troposphere, *J. Atmos. Sci.*, *44*, 1775–1800, 1987.

Meyers, S. D., B. G. Kelly, and J. J. OBrien, An introduction to wavelet analysis in oceanography and meteorology: With application to the dispersion of Yanai waves, *Mon. Weather Rev.*, *121*, 2858–2866, 1993.

Nastrom, G. D., and D. C. Fritts, Sources of mesoscale variability of gravity waves, I, Topographic excitation, *J. Atmos. Sci.*, *49*, 101–110, 1992.

Nastrom, G. D., T. E. VanZandt, and J. M. Warnock, Vertical wavenumber spectra of wind and temperature from high-resolution balloon soundings in the lower atmosphere over Illinois, *J. Geophys. Res.*, *102*, 6685–6701, 1997.

O'Sullivan, D., and T. J. Dunkerton, Generation of inertia-gravity waves in a simulated life cycle of baroclinic instability, *J. Atmos. Sci.*, *52*, 3695–3716, 1995.

Pfister, L. W., S. Scott, M. Loewenstein, S. Bowen, and M. Legg, Mesoscale disturbances in the tropical atmosphere excited by convection: Observations and effects on the stratospheric momentum budget, *J. Atmos. Sci.*, *50*, 1058–1075, 1993.

Reeder, M. J., and M. Griffiths, Stratospheric inertia-gravity waves generated in a numerical model of frontogenesis, II, Wave sources, generation mechanisms and momentum fluxes, *Q. J. R. Meteorol. Soc.*, *122*, 1175–1195, 1996.

Sato, K., A statistical study of the structure, saturation and sources of inertio-gravity waves in the lower stratosphere observed with the MU radar, *J. Atmos. Sol. Terr. Phys.*, *56*, 755–774, 1994.

Sato, K., and M. Yamada, Vertical structure of atmospheric gravity waves revealed by the wavelet analysis, *J. Geophys. Res.*, *99*, 20,623–20,631, 1994.

Sato, K., T. Kumakura, and M. Takahashi, Gravity waves appearing in high-resolution GCM simulation, *J. Atmos. Sci.*, *56*, 1005–1018, 1999.

Schoeberl, M. R., The penetration of mountain waves into the middle atmosphere, *J. Atmos. Sci.*, *42*, 2856–2864, 1985.

Schubert, W., J. J. Hack, P. L. SilvaDias, and S. R. Fulton, Geostrophic adjustment of an axisymmetric vortex, *J. Atmos. Sci.*, *37*, 1464–1484, 1980.

Shimomai, T., M. D. Yamanaka, and S. Fukao, Application of wavelet analysis to wind disturbances observed with MST radar techniques, *J. Atmos. Sol. Terr. Phys.*, *58*, 683–696, 1996.

Smith, R. B., On severe downslope winds, *J. Atmos. Sci.*, *42*, 2597–2603, 1985.

Streten, N. A., The climate of Macquarie Island and its role in atmospheric monitoring, *Pap. Proc. R. Soc. Tasmania*, *122*, 91–106, 1988.

Uccellini, L. W., and S. E. Koch, The synoptic setting and possible energy sources for mesoscale wave disturbances, *Mon. Weather Rev.*, *115*, 721–729, 1987.

Vincent, R. A., Gravity-wave motions in the mesosphere, *J. Atmos. Sol. Terr. Phys.*, *46*, 119–128, 1984.

Vincent, R. A., and D. C. Fritts, A climatology of gravity wave motions in the mesopause region at Adelaide, Australia, *J. Atmos. Sci.*, *44*, 748–760, 1987.

Vincent, R. A., and I. M. Reid, HF Doppler measurements of mesospheric gravity wave momentum fluxes, *J. Atmos. Sci.*, *40*, 1321–1333, 1983.

Vincent, R. A., S. J. Allen, and S. D. Eckermann, Gravity-wave parameters in the lower stratosphere, in *Gravity Wave Processes: Their Parametrization in Global Climate Models*, edited by K. Hamilton, pp. 7–25, Springer-Verlag, New York, 1997.

Warner, C. D., and M. E. McIntyre, Toward an ultra-simple spectral gravity wave parameterization for general circulation models, *Earth Planets Space*, *51*, 475–484, 1999.

Whiteway, J. A., and T. J. Duck, Evidence for critical level filtering of atmospheric gravity waves, *Geophys. Res. Lett.*, *23*, 145–148, 1996.

Whiteway, J. A., and T. J. Duck, Enhanced Arctic stratospheric gravity wave activity above a tropospheric jet, *Geophys. Res. Lett.*, *26*, 2453–2456, 1999.

Yoshiki, M., and K. Sato, A statistical study of gravity waves in the polar regions based on operational radiosonde data, *J. Geophys. Res.*, *105*, 17,995–18,011, 2000.

Zink, F., and R. A. Vincent, Wavelet analysis of stratospheric gravity wave packets over Macquarie Island, 2. Intermittency and mean-flow accelerations, *J. Geophys. Res.*, this issue.

R. A. Vincent and F. Zink, Department of Physics and Mathematical Physics, University of Adelaide, Adelaide 5005, Australia. (robert.vincent@adelaide.edu.au; fzink@physics.adelaide.edu.au)

(Received January 13, 2000; revised November 2, 2000; accepted November 14, 2000.)